Compact scintillator - silicon photomultiplier hard X-ray detectors for laser-plasma diagnosis

Contact: jesel.patel@stfc.ac.uk

J. K. Patel
Loughborough University, LE11 3UE, United Kingdom.

D. Neely, C. D. Armstrong
Central Laser Facility, STFC, OX11 0QX, United Kingdom.

R. J. Clarke, K. Fowell, I. Symonds
Central Laser Facility, STFC, OX11 0QX, United Kingdom.

1 Introduction

Decaying emission of 511 keV annihilation X-rays from materials activated by >3 MeV photons can be used to diagnose laser-plasma interactions [1]. Low-voltage operable silicon-photomultipliers (SiPM) coupled to scintillators are a favourable alternative to large, high voltage photomultiplier tube (PMT) detectors for measuring β^+ annihilations in typically crowded laser target interaction chambers. To improve X-ray collection efficiency and suppress Compton scattering, greater scintillator volumes are required. To optimise its design, the performance of scintillators of varying size is explored, and a simple model is presented which achieves good agreement with the spectra obtained from bismuth germanate (BGO) - SiPM detector combinations tested. In addition, manipulation of the bias voltage of SiPM sensors is shown to readily enable tuning of detector dynamic range, while preserving energy resolution.

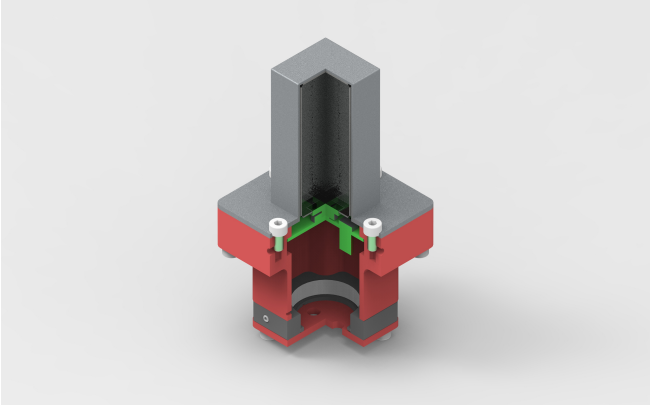

Figure 1: Quarter cut-out design image of a BGO - SiPM detector, with a 25×25×60 mm^3 crystal, ∼ 0.3 mm of PTFE reflective wrapping and a 12×12 mm^2 coupled SiPM array. The detector is housed in vacuum compatible EMP shielding.

2 Energy resolution and scintillator surface area

Large scintillator crystals can increase X-ray collection efficiency, and suppress Compton scattering contributions to spectra by increasing the fraction of X-ray photons which are completely absorbed. However, increasing a scintillator's surface area results in weaker optical signals from a coupled sensor, due to an increase in the average number of internal reflections undergone before detection.

Table 1 gives the resolution and range achieved with a variety of detector systems, and fig. 1 illustrates the design of a SiPM coupled scintillator detector. Increased amplifier gain is required with larger volume detectors to make signals observable with the Kromek Multi-Channel Analyser (MCA) used. Previous work by the author reported in References [2, 3] has identified Cremat charge-sensitive preamplifiers (CSPs) which operate optimally with SiPM-MCA systems.

Weaker SiPM signals correspond to fewer detected optical photons, and the Poissonian nature of photon detection dictates that the average signal resolution therefore deteriorates with increased scintillator size. fig. 2 shows that the resolution achieved with BGO scintillators deteriorates with an increasing ratio of scintillator surface area to coupled SiPM area.

Ideal detector resolution

The energy resolution of an ideal scintillator detector is primarily dependent on the number of measured optical photons, due to the Poissonian statistical nature of photon detection. In this ideal case the variance in the number of photons is equal to its expectation value, and hence, the resolution is given by

$$\%\ \text{FWHM} \approx 100 \cdot \frac{2.355}{\sqrt{N}}, \tag{1}$$

where N is the expected number of photons detected at a given X-ray energy.

The number of optical photons detected by a scintillator - SiPM detector is given by the energy deposited by an incident X-ray beam, the scintillator light yield, the photodetection efficiency of the SiPM, ϵ, and the geometry of the scintillator. Ignoring second order scattering effects, the deposited X-ray energy can approximated by Beer's law:

$$E = E_X(1 - e^{-\rho\mu_m\tau}), \tag{2}$$

where E_X is the energy of an incident X-ray, ρ is the scintillator density, μ_m is the X-ray mass-attenuation

Scintillator	Face area (mm^2)	Length (mm)	Surface area (mm^2)	SiPM bias (V)	Amplifier gain	FWHM (%) 511keV	FWHM (%) 1274keV	Range (MeV)
BGO	10 × 10	10	600	30.0	3×	10.2	7.0	0.24 - 8.2
BGO	10 × 10	40	1800	30.0	3×	18.6	12.7	0.38 - 14
BGO	10 × 10	40	1800	30.0	27×	15.6	9.6	0.08 - 1.4
BGO	10 × 10	60	2600	30.0	27×	18.4	10.4	0.085 - 1.8
BGO	25 × 25	60	7250	30.0	27×	17.8	10.9	0.25 - 2.4
BGO	25 × 25	60	7250	29.0	27×	21.7	10.8	0.25 - 3.9
BGO	25 × 25	60	7250	28.0	27×	17.7	11.0	0.29 - 6.6
BGO	25 × 25	60	7250	27.0	27×	20.7	12.2	0.31 - 12.9

Table 1: Range and FWHM of detector systems able to resolve the 511 and 1274 keV photopeaks of a ^{22}Na calibration source. Systems vary by scintillator, crystal size, SiPM bias voltage and charge amplifier used (varying only in gain). All scintillators are coupled to a 12×12 mm^2 16-pixel SiPM, except for the LYSO crystal, which is coupled to a 6×6 mm^2 4-pixel SiPM. All SiPM pixels are connected in parallel. Spectra are observed using a Kromek K102 Multi-channel Analyser.

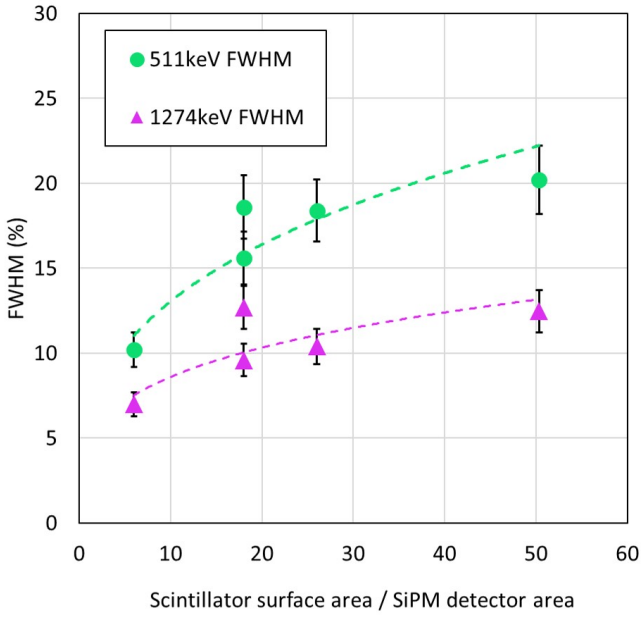

Figure 2: Resolution of 511 and 1274 keV photopeaks of ^{22}Na calibration source by BGO detectors with varying scintillator surface area, with 12×12 mm^2 SiPMs. Dashed lines are power law fits to the data to guide the eye. Error bars are an estimated 10% uncertainty.

coefficient of the scintillator at a given energy E_X, and τ is the path length of the X-ray inside the scintillator, i.e. the scintillator thickness along the X-ray beam path. Assuming a linear response, the number of scintillation photons produced is then

$$N_{scint} = \kappa E, \tag{3}$$

where κ is the light yield of the scintillator in optical photons per MeV deposited. A coupled sensor will only detect a fraction of the total emitted scintillation light, due to imperfect reflectivity of the scintillator coating. A simple model for the fraction of detected light is presented in §4, and gives the number of **detected** photons as

$$N_{det} = E\kappa\epsilon\frac{X'}{1-R-RX'}, \tag{4}$$

where R is the reflectivity of the scintillator surface coating, ϵ is the sensor detection efficiency, and X' is a parameter dependant on the scintillator refractive index, surface area of the crystal and coupled detector area (see Section §4).

Substituting the final number of detected optical photons into Eq. (1), we can predict the optimum resolution of a scintillator detector at a given energy. For a 25×25×60 mm^2 crystal and a 12×12 mm^2 SiPM array, around 15% of the total scintillation photons are incident to the SiPM array. For a Ketek 25 μm microcell SiPM array, the photodetection efficiency at the peak emission of BGO (480 nm) is around 37%, and a BGO scintillator has a light yield of around 9 photons per keV. Assuming 511 keV X-rays deposit completely, the number of detected photons from a 511 keV X-ray can be calculated as

$$N_{det} = 511 \times 9 \times 0.15 \times 0.37 \approx 255 \text{ photons}. \tag{5}$$

The theoretical minimum resolution is then

$$\%\ \text{FWHM} = 100 \cdot \frac{2.355}{\sqrt{255}} \approx 14.7\%. \tag{6}$$

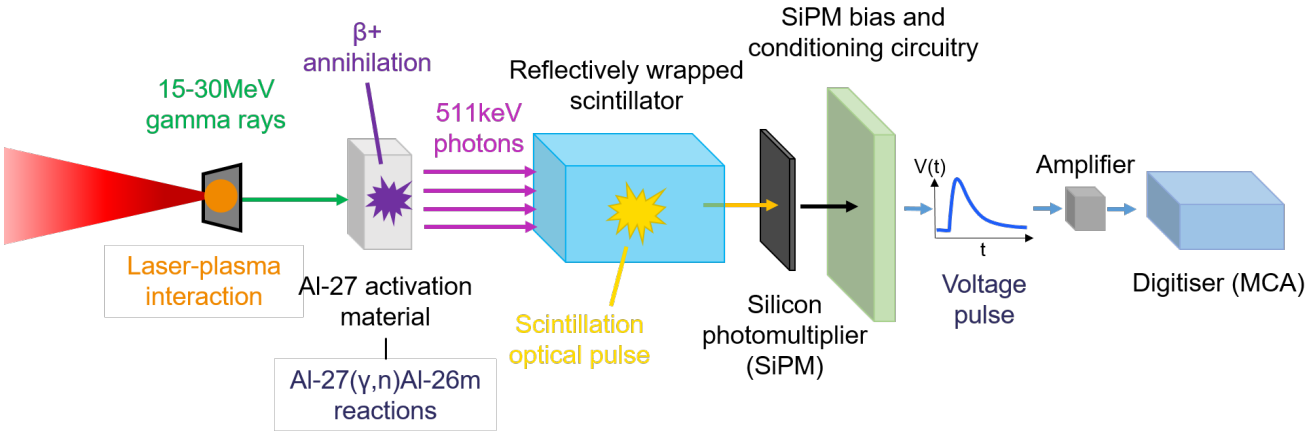

Figure 3: Schematic of scintillator - SiPM detector for gamma counting diagnostic using activation of ^{27}Al

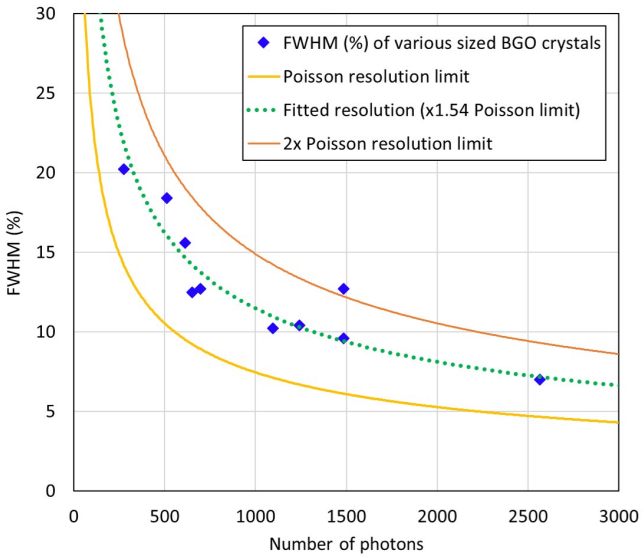

Figure 4: Measured resolutions of 511 and 1274 keV ^{22}Na peaks with BGO crystals of sizes from 10×10×10 mm^3 to 25×25×60 mm^3 as a function number of photons detected (calculated using absolute calibration of 25 μm microcell Ketek SiPM at 30 V bias voltage by A. Dasgupta [6]). The Poisson statistical resolution limit (see Eq. (1)) is the solid yellow line, and the solid orange line is this limit multiplied by a coefficient of 2. Fitting to the measured data yields a coefficient of 1.54, where the data has a sample deviation from the fit of $s = 1.67\%$, and 90% of the measured points lie within 1-2× the Poisson resolution limit.

Comparing with the results obtained in Table 1, it is evident that this resolution is not achieved for 511 keV X-rays using a ^{22}Na source. This is due to the additional noise contributions from the intrinsic scintillator yield variance, and the variance in the SiPM gain and digitisation electronics. The achieved resolutions with various size BGO crystals are shown as a function of number of detected photons, along with the ideal Poissonian resolution, in Fig. 4.

Figure 5 shows the limit imposed by the optical light yield on the resolution achieved by different scintillator materials. In practice, detectors are unlikely to achieve this limit, due to additional variance in the final signal caused by multiple factors. These include, but are not limited to: variance in the light yield of the scintillator, caused by thermal and non-proportionality effects (scintillator intrinsic resolution); optical scattering or absorption in the scintillator; variation in the gain of the optical sensor; noise contributions by the amplification and digitisation electronics; and dark counts in the optical sensor due to thermal excitations.

Resolution of 583 keV X-rays from a ^{232}Th source using a 25×25×60 mm^3 BGO - SiPM detector at 18.6°C and -11.9°C are shown in fig. 6. A small improvement in resolution achieved by reducing the temperature. This is largely due to the strong temperature dependence of the yield of the BGO scintillator used, resulting in better photon statistics at lower temperatures [4], reducing the Poisson limit. The increased signal at lower temperatures is evident in the raw spectra shown in fig. 7. Reduction in thermal noise in the SiPM will also contribute a small amount to the improved resolution at lower temperatures.

3 Tuning dynamic range with SiPM bias voltage

The intrinsic gain of SiPMs scales linearly with 'overvoltage'; the amount by which the applied bias voltage is greater than the breakdown voltage [5]. By reducing

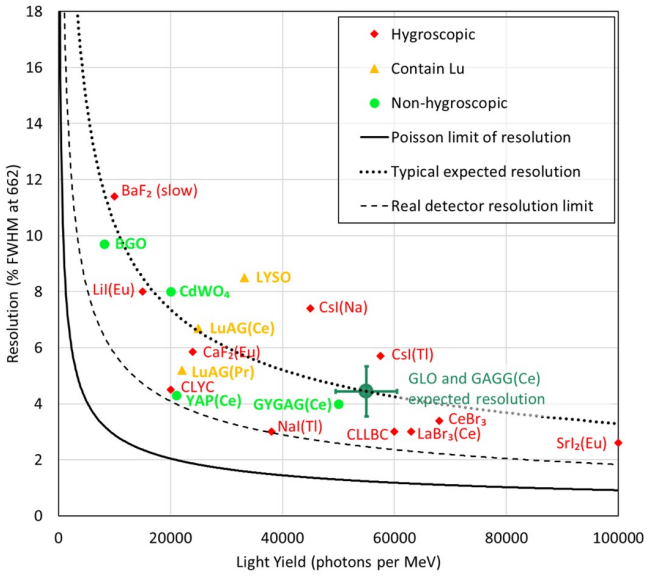

Figure 5: Measured resolutions at 662 keV by X-ray scintillators from References [4, 7–19]. Solid line is Eq. (1) with $N = N_{scint}$, the scintillator light yield per deposited X-ray energy in MeV. Dashed line is Eq. (1) with $N = N_{det}$, using a 50% sensor efficiency, ϵ, and a 50% cavity efficiency (i.e. the fraction of X' in Eq. (4)). The dotted line is 1.8× the dashed line, to guide the eye through surveyed resolution data.

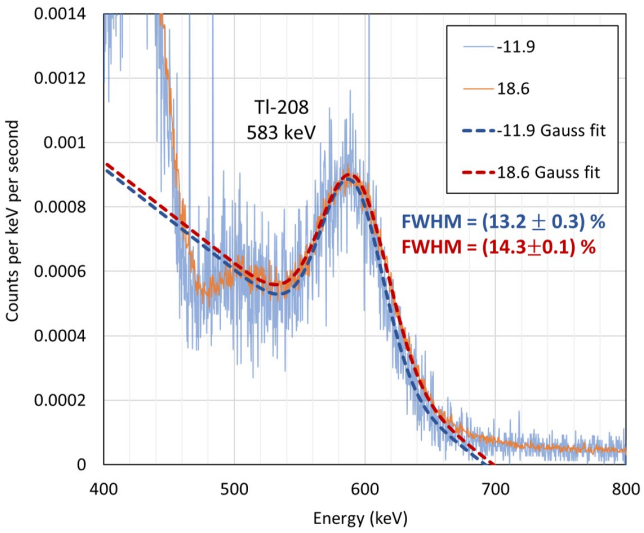

Figure 6: Resolution of 583 keV X-rays from ^{232}Th to ^{208}Tl decay, using a 25×25×60 mm^3 BGO - SiPM detector at 18.6°C (1040 sec acquisition) and -11.9°C (101 sec acquisition). FWHM obtained by fitting a Gaussian superposed on a linear background, shown with estimated uncertainties.

the bias, and subsequently the overvoltage, the size of the output signals can be lowered, without affecting the number of detected photons. For digitisation electronics with a finite dynamic range, this means that the bias voltage applied to the SiPM can be used to tune the output of the detector to optimise the observed range of X-ray energies for a given configuration.

The charge amplifiers used in this work saturate at output amplitudes in excess of 1.50 V. A 16-pixel SiPM at 30 V bias becomes significantly non-linear above 530 mV output pulse amplitudes, so with the amplifier gains $\geq 3\times$, the upper signal range is constrained by the amplifier saturation.

The dynamic range of the detector at different bias voltage is shown in fig. 8 (inset), as limited by the 27 × gain CR-112 amplifier's saturation limit. While the range is greatest at 27 V bias, operating the SiPM this close to the breakdown voltage ($\approx$ 24.5 V at $\sim$ 20 °C) causes it to respond non-linearly, resulting in signal inhibition shown in the energy spectrum at 27 V bias in fig. 8. Despite this, significant tuning of the range is still possible without excessive loss of signal, and it is evident in fig. 8 that energy resolution is excellently preserved across 3 - 5.5 V overvoltage.

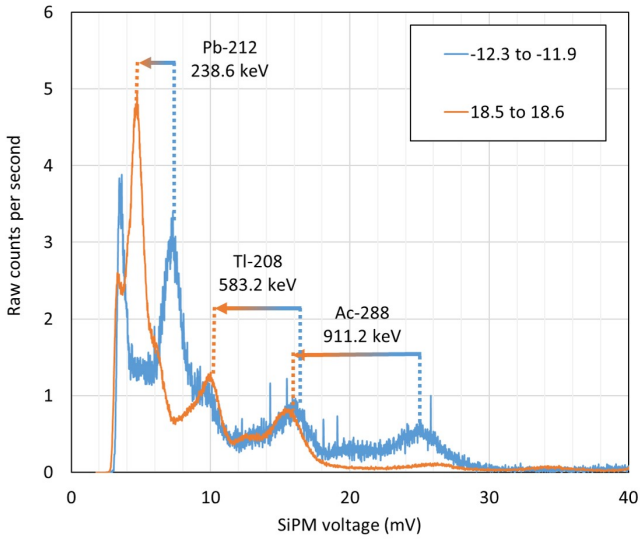

Figure 7: Raw Th-232 spectra using a 25×25×60 mm^3 BGO - SiPM detector at 30 V bias voltage. Spectra measured at 18.6°C (1040 sec acquisition) and -11.9°C (101 sec acquisition). X-ray photopeaks can be seen to shift to lower voltage readouts as the bias voltage of the SiPM increases with the temperature, subsequently reducing the overvoltage and SiPM intrinsic signal gain.The higher temperature acquisition has larger apparent peaks due to smaller signal dispersion across digitisation channels, and increased background signal.

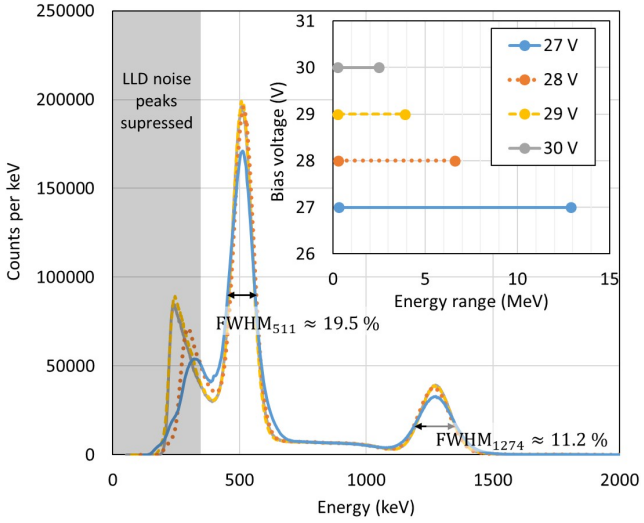

Figure 8: ^{22}Na spectra obtained with 25×25×60 mm^3 BGO crystal coupled to 12×12 mm^2 SiPM array at four bias voltages. Grey shaded region illustrates lower-level discriminator (LLD) suppressed region, set in different channels for different bias voltage acquisitions to best suppress noise, which lead to mismatched spectral data $<$ 300 keV. 511 keV and 1274.5 keV ^{22}Na peaks are shown with close to identical resolution for bias voltages in the range 28 - 30 V, and response appears to fall off at 27 V. 15 hr acquisitions using CR-112 amplifier and Kromek MCA. Inset shows detector energy range due to limiting amplifier and noise floor at bias voltages.

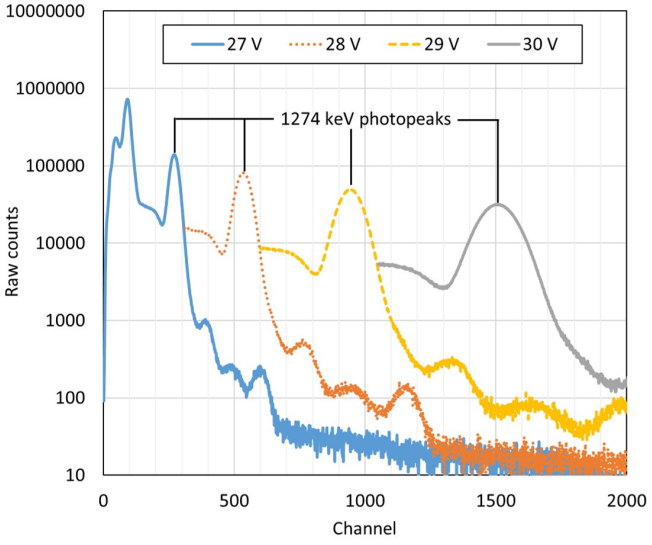

Figure 9: Raw ^{22}Na spectra obtained with 25×25×60 mm^3 BGO crystal coupled to 12×12 mm^2 SiPM array at four bias voltages, showing the shift in the 1274 keV photopeak as the bias is varied. Lower channels of 28 - 30 V spectra are omitted for clarity. Note that the y-axis is logarithmic.

4 Modelling scintillator detectors as cavities

For a given area of optical sensor (i.e. SiPM), signal amplitudes are observed to fall across scintillators increasing size. Considering the first five BGO detectors in Table 1 with identical SiPMs at 30 V bias, we can determine the physical parameters contributing to this effect, by fitting a model of detected signal amplitude with varying scintillator size.

To construct our model, we consider the evolution of the number of photons in a spherical cavity with Lambertian scattering surfaces of some reflectivity, R, and total surface area, A_{scint}. This represents the scintillator and its reflectively wrapped surfaces. There is some area of the cavity surface which corresponds to the transmissive 'exit face' with an area, A_{exit}, which is coupled to our SiPM optical sensor. For an ideal scintillator, the initial number of photons in the cavity, $N_{cav,0}$, is proportional to deposited X-ray energy, with some constant of proportionality, κ, representing the efficiency of the scintillator, in units of photons per MeV;

$$N_{cav,0} = N_{scint} = \kappa E. \tag{7}$$

Assuming isotropic scintillation from the centre of a spherical scintillator, the optical flux incident to the surfaces of a crystal can be considered to be uniform. Hence, the fraction of photons in the cavity which will be incident on the exit face is the ratio of the surface areas:

$$X = \frac{A_{exit}}{A_{scint}}, \tag{8}$$

and the number of photons which initially exit the cavity is

$$N_{exit,0} = XN_{cav,0} = XN_{scint} \tag{9}$$

The fraction of photons which are not lost through the exit face is the quantity $1-X$. These photons are incident to the reflective cavity surfaces, and either transmitted through with probability T, or diffusely reflected back into the cavity with probability $R = 1 - T$. The number of photons remaining inside the cavity after one internal reflection is

$$N_{cav,1} = RN_{cav,0}(1 - X) = RN_{scint}(1 - X) \tag{10}$$

Assuming these photons are also isotropic and omnidirectional, the same fraction, X, will be incident to the exit face, and the subsequent exiting number of photons is

$$N_{exit,1} = XN_{cav,1} = XRN_{scint}(1 - X) \tag{11}$$

Once again, the fraction $1 - X$ of photons which remain in the cavity will either be transmitted and lost, or internally reflected with probability R. The number of photons remaining in the crystal after a second internal reflection ($n = 2$), is

$$N_{cav,2} = R(N_{cav,1} - N_{exit,1}). \tag{12}$$

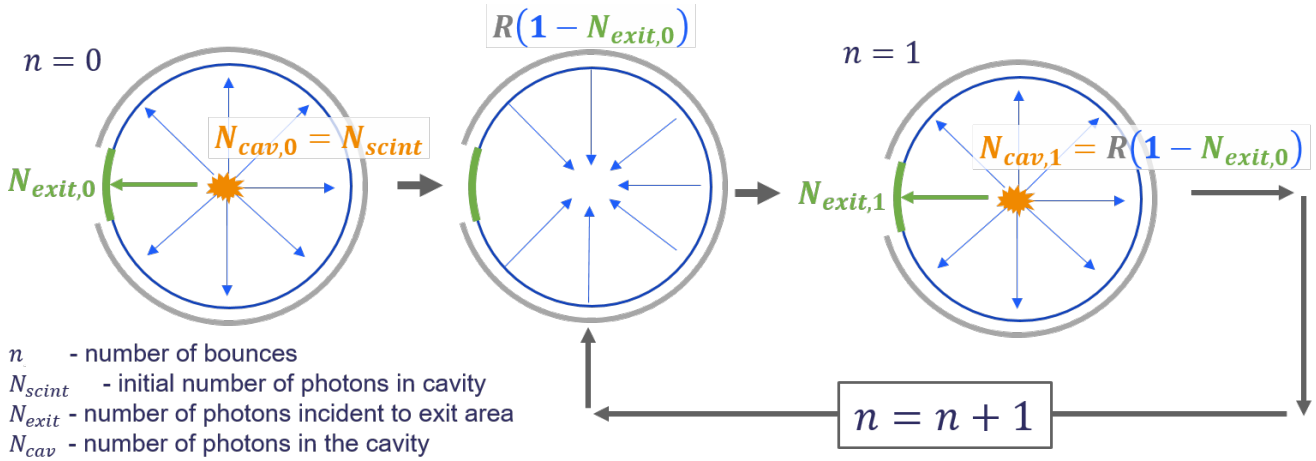

Figure 10: Schematic of simple cavity model to predict scintillator output signal behaviour

Substituting Eqs (10) and (11),

$$N_{cav,2} = N_{scint}R^2(1-X)^2, \tag{13}$$

and the output signal is

$$N_{exit,2} = XN_{cav,2} = XN_{scint}R^2(1-X)^2 \tag{14}$$

By comparison of Eqs (9), (11) and (14), we obtain the geometric series

$$\begin{aligned} &XN_{scint} + XN_{scint}R(1-X) \\ &\quad + XN_{scint}R^2(1-X)^2 + ... \\ &\qquad ... + XN_{scint}R^{n-1}(1-X)^{n-1} \\ &\qquad\quad + XN_{scint}R^n(1-X)^n \end{aligned}$$

$$= XN_{scint}\sum_{m=0}^{M}(R(1-X))^m. \tag{15}$$

As $M \longrightarrow \infty$, we obtain the total number of photons transmitted through the exit face,

$$N_{trans} = XN_{scint}\sum_{m=0}^{\infty}(R(1-X))^m \tag{16}$$

$$= \frac{XN_{scint}}{1-R(1-X)} \tag{17}$$

$$= \frac{XN_{scint}}{1-R+RX}. \tag{18}$$

Equation (18) gives a simple vacuum model for the optical output from a reflective cavity, based on the surface areas of the cavity and the exit face, and assuming perfect transmission through the exit face. However, a real system is composed of a coupling of two materials at the exit face, with finite optical densities. If we assume the surfaces are anti-reflective coated, we can ignore Fresnel reflection effects, and this boundary is then described by the refractive indices of the scintillator, n_1, and SiPM glass window, n_2. Snell's law states that rays incident to a boundary of media with differing refractive index are only transmitted when their angle of incidence is smaller than the critical angle, defined as

$$\sin\psi_{crit} = n_2/n_1 \tag{19}$$

A first order approximation gives

$$\psi_{crit} \approx n_2/n_1, \tag{20}$$

which underestimates ψ_{crit} by 5-10% at large angles (due to Fresnel losses at these angles in a real system, this is acceptable for this simple model). Equation (20) gives an acceptance cone for exiting photons, such that the fraction of isotropic incident photons which are transmitted is the solid angle of the acceptance cone, over the hemispherical solid angle, 2π,

$$\frac{\Omega_{crit}}{2\pi} = \frac{2\pi(1-\cos\psi)}{2\pi} \tag{21}$$

$$\approx (1-(1-\frac{\psi_{crit}^2}{2})) \tag{22}$$

$$\approx \frac{n_2^2}{2n_1^2}. \tag{23}$$

We can describe the equivalent optical surface area of the exit face as

$$A'_{exit} = A_{exit}\frac{n_2^2}{2n_1^2}, \tag{24}$$

and the cavity,

$$A'_{scint} = A_{scint} - A_{exit}(1-\frac{n_2^2}{2n_1^2}). \tag{25}$$

Now, with our effective optical surface areas, the fraction of photons in the cavity which are incident to the effective exit face is

$$X' = \frac{A'_{exit}}{A'_{scint}}, \tag{26}$$

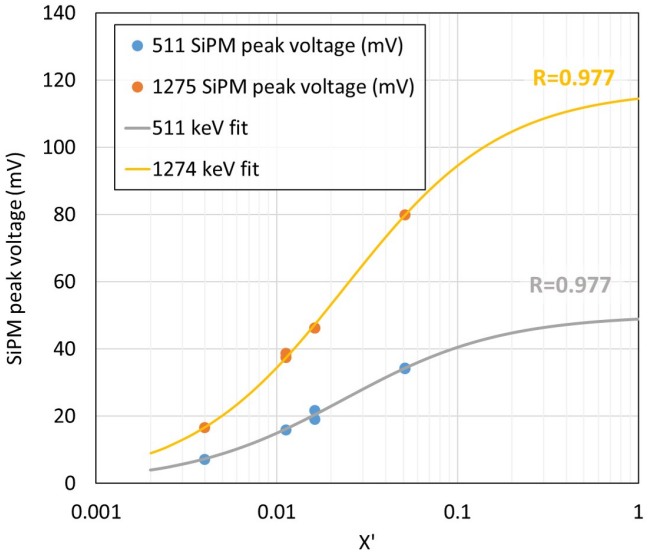

Figure 11: Fitting of equation (28) to the 511 and 1274 keV signals obtained with the five BGO detectors at 30 V bias listed in Table 1, with obtained values for the reflectivity, R, labelled. Signals were corrected for the gain of the amplifiers used.

and the total number of photons transmitted through the exit face is

$$N_{trans} = \frac{X' N_{scint}}{1 - R + RX'}. \tag{27}$$

A SiPM has a linear response for low intensities, so the peak voltage output in milli-volts is

$$V_{peak} = \frac{X' N_{scint} \epsilon g}{1 - R + RX'}, \tag{28}$$

where ϵ is the photodetection efficiency, and g is signal gain in mV per detected photon.

Equation (27) is fitted to the 511 and 1274 keV signals obtained with the five BGO detectors at 30 V bias listed in Table 1, shown in fig. 11. Refractive index values used for BGO and the SiPM glass window are 1.79 [4] and 1.52 [5], respectively. Fitting parameter R^2 values of unity are obtained to 2 and 3 significant figures for the 511 keV and 1274 keV signals, respectively. Values of ≈98% for the reflectivity of the PTFE wrapped crystals are produced by both fits. These are in agreement with expected values for 3-4 layers of the 0.2 mm thick tape used, from measurements by M. Janecek [20] made with an integrating sphere set up. The model is expected to underestimate the real reflectivity due to its basis on a spherical cavity geometry, with isotropic and omnidirectional behaviour of optical photons. Crystals with cuboid or other geometries require further corrections to model their behaviour more precisely. However, the model is consistent with the signals obtained from events at two energies, with detectors of various dimensions and amplification, and is a simple predictive tool which is useful for future detector design, such as in a pixelated array for X-ray radiography, as discussed in J. K. Patel et al., CLF Annual Reports 2020 [21].

5 Conclusion

Dynamic range and resolution of scintillator - SiPM detectors has been investigated based on systems which resolve the 511 and 1274 keV X-ray emissions from ^{22}Na. Resolution is limited by and is generally dominated by Poissonian statistics, with increased detector size leading to lower resolution due to less efficient optical detection. It is demonstrated that the dynamic range of detectors can be tuned by varying SiPM bias voltage, without significant loss of resolution. A simple model is presented for signal output, which treats a scintillator as a spherical cavity, achieving a good fit with empirical results and consistency across the two ^{22}Na photopeaks. However, more complex modelling is required to better account for the impact of non-spherical geometries (particularly sharp vertices) on obtained signals.

6 Appendix

The cavity model presented in §4 makes the assumption that the photons from the intial emission from a scintillation event behave in the same way to photons which are subsequently reflected in the cavity. However, if the exit face of the cavity subtends a significant cone of the emission, there may be a significantly different contribution to the total fraction of exiting light. Figure 12. illustrates two conditions: where the cone of transmission (i.e. with half-angle given by the critical angle of the boundary) is smaller than the exit face area; and where it is larger. If we assume that the average depth if the intial scintillation emission occurs half-way through the crystal depth, $\tau/2$, then the boundary between the two conditions is at

$$\tau \approx \frac{2pn_2}{n_1\sqrt{\pi}}, \tag{31}$$

where p is the lateral scintillator dimension, as shown in fig. 12. In the first case, where $\tau < \frac{2pn_1}{n_2\sqrt{\pi}}$, the fraction of the initial scintillation emission which directly exits the cavity is given by the fractional solid angle of the entire cone:

$$\frac{N_{exit,0}}{N_{scint}} = \frac{2\pi(1 - \cos(\psi_{crit.}))}{4\pi}, \tag{32}$$

$$\approx n_2^2/4n_1^2, \tag{33}$$

using Snell's law and the paraxial approximations of the sine and cosine functions. In the second case, $\tau > \frac{2pn_2}{n_1\sqrt{\pi}}$, the fraction is the fractional solid angle subtended by the

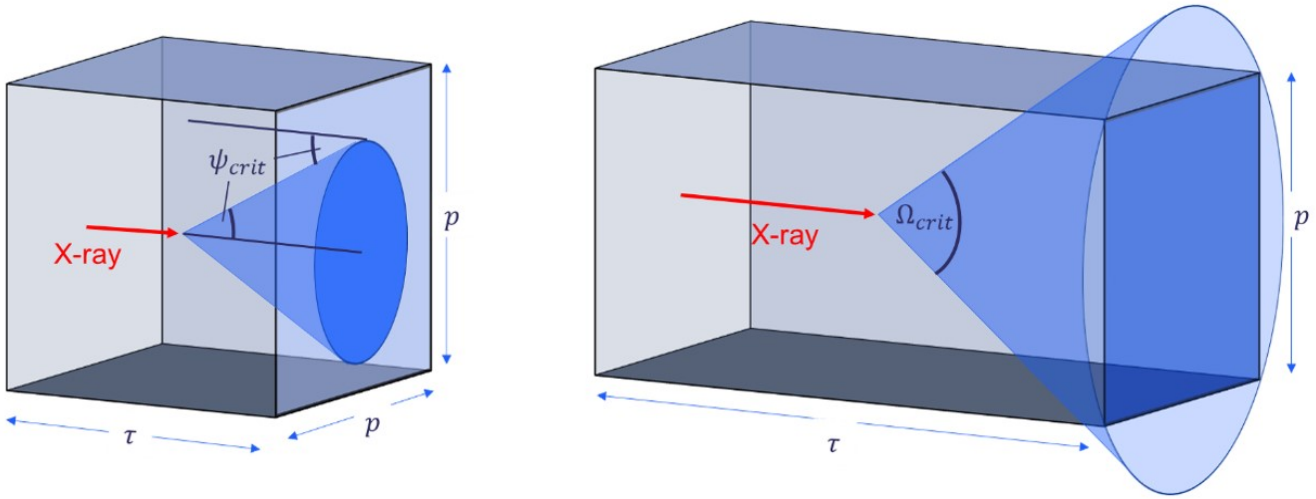

Figure 12: Immediate exit cone for X-ray deposited at $\tau/2$ into crystal, for depth $\tau < \frac{2pn_1}{n_2\sqrt{\pi}}$ (left), and $\tau > \frac{2pn_1}{n_2\sqrt{\pi}}$ (right).

$$\frac{N_{exit}}{N_{scint.}} = \frac{n_2^2}{4n_1^2} + X'\left(1 - \frac{n_2^2}{4n_1^2}\right)\frac{R}{1-R+RX'}, \qquad \text{for} \quad \tau < \frac{2pn_1}{n_2\sqrt{\pi}} \tag{29}$$

$$\frac{N_{exit}}{N_{scint.}} = \frac{p^2}{\pi\tau^2} + X'\left(1 - \frac{p^2}{\pi\tau^2}\right)\frac{R}{1-R+RX'}, \qquad \text{for} \quad \tau > \frac{2pn_1}{n_2\sqrt{\pi}}. \tag{30}$$

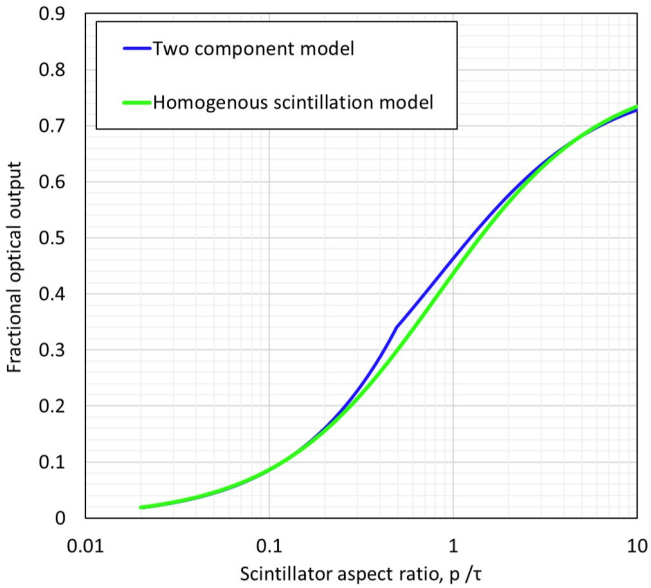

Figure 13: The fractional optical output, $N_{exit}/N_{scint.}$, given by two cavity models, plotted as a function of the aspect ratio of the lateral dimension, p, to the depth, *tau*. A $\tau = 1$ mm scintillator with refractive index of LYSO ($n_1 = 1.81$), immersed in air ($n_2 = 1$), and with a coating equivalent to 0.1 mm PTFE ($R = 0.88$) was simulated across varying lateral size, p, to simulate the behaviour of a pixel in an array configuration.

exit face at the emission depth.

$$\frac{N_{exit,0}}{N_{scint}} = \frac{\Omega_{exit}}{4\pi}, \tag{34}$$

$$\approx \frac{A_{exit}}{4\pi(\tau/2)^2}, \tag{35}$$

$$\approx \frac{p^2}{\pi\tau^2}. \tag{36}$$

Following the same assumptions as the simpler model in §4 for light subsequently rebounding in the cavity, we arrive at a model which better accounts for the behaviour of immediately exiting light, by splitting it into the two regimes outlined above; where the scintillator thickness is relatively thin compared with its lateral size, and where it is relatively thick. This 'two component' version of the cavity model is given in Eqs. (29) and (30), and is plotted with the original homogeneous scintillation cavity model in fig. 13 for a specific case. It is clear that there is a maximum deviation of $\approx 0.05N_{scint.}$ of the homogenous scintillation model from the two-component model when $p \approx 2\tau$. This deviation is reduced when the reflectivity of the coating of the cavity is increased to 98%, so the simpler homogeneous scintillation model is sufficient in these conditions.

References

[1] R. J. Clarke et al. , 2006 *Detection of short lived radioisotopes as a fast diagnostic for intense laser-solid interactions* Appl. Phys. Lett. **89**, 141117 (2006)

[2] J.K. Patel et al., 2019 *Gain characterisation of RF amplifiers for a silicon photomultiplier - scintillator gamma ray detector.* Central Laser Facility, STFC, Rutherford Appleton Laboratory.

[3] J. K. Patel, C. D. Armstrong and D. Neely, 2019 *Performance of a Kromek multi channel analyser for a silicon photomultiplier - scintillator gamma ray detector* CLF, STFC, Rutherford Appleton Laboratory.

[4] Saint-Gobain Ceramics & Plastics, Inc, *Bismuth germanate scintillation material datasheet* https://www.crystals.saint-gobain.com/sites/imdf.crystals.com/files/documents/bgo-material-data-sheet.pdf

[5] KETEK GmbH., *Device Parameters* https://www.ketek.net/sipm/technology/device-parameters/

[6] A. Dasgupta, 2019 *Detection and spectral analysis of X-ray radiation from laser plasma interactions.* University of Bristol.

[7] J. Glodo et al., *New Developments in Scintillators for Security Applications* Physics Procedia Volume 90, Pages 285-290, 2017, https://doi.org/10.1016/j.phpro.2017.09.012

[8] S. Derenzo, M. Boswell, M. Weber, K. Brennan, *Scintillation Properties* Lawrence Berkeley National Laboratory http://scintillator.lbl.gov/ Accessed June 2020

[9] M. J. Cieślak, K. A. A. Gamage, R. Glover, *Critical Review of Scintillating Crystals for Neutron Detection* Crystals 2019, **9(9)**, 480 https://doi.org/10.3390/cryst9090480

[10] N. J. Cherepy et al., *Transparent Ceramic Scintillators for Gamma Spectroscopy and MeV Imaging* Proc. SPIE 9593, Hard X-Ray, Gamma-Ray, and Neutron Detector Physics XVII, 95930P (4 September 2015), https://doi.org/10.1117/12.2189156

[11] Advatech Ltd., *Lutetium Aluminium Garnet (Ce)* and *Yttrium Aluminium Perovskite (Ce)*, https://www.advatech-uk.co.uk/scintillators-crystals_a_c.html , Accessed June 2020

[12] W. Chewpraditkul et al., *Scintillation Properties of LuAG:Ce, YAG:Ce and LYSO:Ce Crystals for Gamma-Ray Detection* IEEE Trans. Nucl. Sci., **56**(6), (2009) https://doi.org/10.1109/TNS.2009.2033994

[13] Cherepy, N., Payne, S., Sturm, B., O'Neal, S., Seeley, Z. et al., *Performance of europium-doped strontium iodide, transparent ceramics and bismuth-loaded polymer scintillators* Proc. SPIE. 8142, Hard X-Ray, Gamma-Ray, and Neutron Detector Physics XIII https://doi.org/10.1117/12.896656

[14] Scionix Holland BV., *Scintillation Crystals: Mechanical, optical and scintillation properties* https://scionix.nl/scintillation-crystals/#tab-id-4

[15] B. Seitz, N. Campos Rivera and A. G. Stewart, *Energy Resolution and Temperature Dependence of Ce:GAGG Coupled to 3 mm × 3 mm Silicon Photomultipliers* IEEE Trans. Nucl. Sci., vol. 63, no. 2, pp. 503-508, April 2016, https://doi.org/10.1109/TNS.2016.2535235

[16] L. Swidervski, M. Moszynski, A. Nassalski et al., *Light Yield Non-Proportionality and Energy Resolution of Praseodymium Doped LuAG Scintillator* IEEE Trans. Nucl. Sci., vol. 56, pp. 934-938, July 2009, https://doi.org/10.1109/TNS.2009.2015590

[17] F. Danevich, A. Georgadze, V. V. Kobychev et al., *Application of PbWO4 crystal scintillators in experiment to search for 2-beta decay of 116Cd* Nucl. Instrum. Meth. A, vol 556, issue 1, pg 259-265, 2006, https://doi.org/10.1016/j.nima.2005.09.049

[18] K. S. Shah, J. Glodo, W. Higgins, E. V. D. van Loef, W. W. Moses et al., *CeBr3 Scintillators for Gamma-Ray Spectroscopy* IEEE Trans. Nucl. Sci., vol. 52, no. 6, pp. 3157-3159, Jan 2006 https://doi.org/10.1109/TNS.2005.860155

[19] D. S. McGregor, 2018 *Materials for Gamma-Ray Spectrometers: Inorganic Scintillators* Annual Review of Materials Research **48, 1**, 245-277. DOI: https://doi.org/10.1146/annurev-matsci-070616-124247

[20] M. Janecek, 2012 *Reflectivity Spectra for Commonly Used Reflectors* IEEE Transactions on Nuclear Science **59, 3**, 490-497. DOI: 10.1109/TNS.2012.2183385

[21] J.K. Patel et al., 2020 *Scintillator imaging for high rep-rate radiography* Central Laser Facility, STFC, Rutherford Appleton Laboratory.